Materials & Design 268 (2026) 116578

Contents lists available at ScienceDirect

Materials & Design

journal homepage: www.elsevier.com/locate/matdes

Cyclic temperature-dependent response of unit cell auxetic structures in an additively manufactured shape memory alloy

Emanuele Avoledo [a,*], Xiebin Wang [b], Jiawen Xu [b], Federico Scalzo [a], Enrico Salvati [a,*]

[a] Polytechnic Department of Engineering and Architecture, University of Udine, Via delle Scienze 206, Udine, Italy
[b] State Key Laboratory of Advanced Equipment and Technology for Metal Forming, Shandong University, Jinan 250061, China

ARTICLE INFO

Keywords:
Auxetic structures
NiTi
Additive manufacturing
Superelasticity
X-ray μ-computed tomography

ABSTRACT

This study investigates the mechanical response of additively manufactured NiTi sinusoidal hexagonal re-entrant auxetic structures, focusing on the combined influence of temperature and local geometry. The NiTi alloy fabricated by laser powder bed fusion (L-PBF) was thermomechanically characterised to identify conditions promoting enhanced superelastic response, while X-ray micro-computed tomography was used to assess internal porosity.

Monotonic and strain-controlled cyclic tensile tests were performed on auxetic cells with three different fillet radii, using a dedicated setup combining digital image correlation and closed-loop temperature control.

The results reveal a clear separation between material- and geometry-driven effects. Temperature primarily governs the load levels through the superelastic response of the alloy, whereas auxetic deformation behaviour and failure mechanisms are mainly controlled by the structural geometry, particularly the fillet radius. Increasing the fillet radius significantly affects the deformation and failure response of the auxetic structures, altering the relationship between failure strain and absolute displacement through the corresponding change in cell geometry.

The experimentally measured Poisson's ratio was compared with predictions from analytical models. Although these overestimate the auxetic response, they provide a reasonable first-order estimate. These findings provide insight into the design of additively manufactured NiTi auxetic architectures.

1. Introduction

Auxeticity is the property of a material that expands (contracts) laterally under uniaxial tension (compression). This property is characterised by a negative Poisson's ratio (NPR). The possibility for a material to show an NPR remained a theoretical consideration for decades [1] until Gibson and Ashby predicted and experimentally observed an NPR in 2D cellular solids with a honeycomb structure [2]. Subsequently, Lakes, in a pioneering work in 1987 [3], obtained polymer and metallic foams that exhibited isotropic NPR, demonstrating that auxetic behaviour can be achieved in a conventional material by modifying the manufacturing process. Evans, who also coined the term auxetic in 1991, was among the first scientists to focus on the manufacture of auxetic polymers and composites and on their real-world application [4]. From this point onward, interest in auxetic materials increased considerably [5]. Since Poisson's ratio and elastic modulus are related to the bulk and shear moduli, having an NPR enables the appearance of unusual properties such as higher indentation resistance, higher fracture toughness, and the ability to deform out-of-plane with a synclastic curvature [6]. In nature, few materials exhibit an NPR; among those are α-cristobalite [7] and various biological tissues [8]. Thus, it was necessary to artificially create auxetic materials, which can be classified as a specific branch of mechanical metamaterials. The properties of metamaterials, which are unusual with respect to natural materials, can be achieved through appropriate internal structuring and designed geometry [9]. In this context, additive manufacturing enables the fabrication of auxetic metamaterials whose mechanical behaviour is governed by their internal architecture rather than by the base material. The layer-by-layer process enables the accurate realisation of designed auxetic unit cells in polymeric and metallic systems, supporting experimental investigations of their mechanical properties [10,11].

Auxetic behaviour can be achieved through a wide range of unit-cell geometries, including re-entrant, chiral, rotating, and perforated architectures, implemented in both lattice-based and thin-sheet systems

* Corresponding authors.
E-mail addresses: avoledo.emanuele@spes.uniud.it (E. Avoledo), enrico.salvati@uniud.it (E. Salvati).

https://doi.org/10.1016/j.matdes.2026.116578
Received 17 April 2026; Received in revised form 11 June 2026; Accepted 9 July 2026
Available online 10 July 2026

[12–15]. Despite this variety, existing designs often present limitations related to anisotropy, stress concentration, or restricted strain ranges, motivating the development of novel auxetic topologies with improved performance [16]. Recent efforts toward unified design and classification frameworks further highlight that the systematic exploration of new auxetic geometries remains an open research field [17].

Auxetic structures have been explored in a variety of application areas that exploit their negative Poisson's ratio and associated mechanical properties. Applications include biomedical devices and tissue engineering scaffolds, where auxetic architectures can improve mechanical compatibility and implant–tissue interaction [18,19], as well as impact mitigation and energy-absorption systems for protective and defence applications [20,21]. Auxetic metamaterials have also been investigated in smart material systems incorporating sensing, actuation, or adaptive functionalities [5,22].

The integration of auxetic architectures with shape memory alloys (SMA) represents a further step toward functional, active auxetic metamaterials. Auxetic NiTi lattice structures fabricated by additive manufacturing (AM) have been shown to combine negative Poisson's ratio with superelastic or shape memory behaviour, enabling recoverable deformation and geometry-dependent tuning of stiffness and compliance [23,24]. These characteristics are relevant for biomedical and smart structural applications, including implantable devices such as stents and orthopaedic implants, where mechanical compatibility, controlled deformation, and reduced stiffness mismatch are required [25]. More recently, SMA-based auxetic metamaterials have been proposed as active systems capable of thermally or electrically driven actuation, linking auxetic deformation mechanisms with programmable mechanical functionality [5,26].

SMAs are metallic materials characterised by a reversible martensitic phase transformation, which gives rise to the shape memory effect (SME) and superelasticity (SE). While the SME involves strain recovery upon heating, SE occurs under isothermal mechanical loading at temperatures above the austenite finish temperature A_f, enabling large, fully recoverable strains through stress-induced martensitic transformation [27–29]. Among SMAs, near-equiatomic NiTi alloys are the most widely investigated, owing to their stable SE response and ability to sustain large cyclic strains [30]. The associated stress–strain hysteresis, low effective stiffness, and high energy dissipation are particularly relevant for architected and lattice-based structures subjected to repeated deformation. Under cyclic loading, the mechanical response of SMAs is governed by both structural and functional fatigue. Structural fatigue is associated with microstructural damage accumulation and eventual failure, whereas functional fatigue refers to the progressive degradation of SE behaviour, including reduced recoverable strain and evolving transformation stresses due to the stabilisation of martensite during cycling [31–33].

AM enables the fabrication of NiTi components with complex geometries that are difficult to achieve using conventional processing routes, supporting the development of architected and lattice-based structures. However, the AM of NiTi remains challenging due to the high sensitivity of transformation behaviour to composition, thermal history, and processing conditions [34]. Issues such as Ni evaporation, oxidation, compositional inhomogeneity, and process-induced defects can significantly affect transformation temperatures, SE stability, and fatigue performance, often requiring careful process optimisation and post-processing treatments [35,36].

Auxetic metamaterials based on AM combine the auxetic response enabled by architectural freedom and manufacturing technology with the intrinsic ability of SMAs to undergo significant recoverable deformation. Being able to reliably exploit and predict the quasi-static and cyclic response of these systems is fundamental for the development of engineering devices with unprecedented structural and functional characteristics. Recent studies have investigated NiTi architected structures combining auxetic geometries with the functional behaviour of shape memory alloys. Dengiz et al. [37] analysed NiTi auxetic thin-film structures, showing that the reversible martensitic transformation enables large recoverable deformations while preserving the auxetic deformation mechanism. Similarly, Biffi et al. [38] examined the microstructural and mechanical response of NiTi lattice structures produced by Laser Powder Bed Fusion (L-PBF), highlighting the influence of AM on the functional behaviour of the alloy. More recently, architected NiTi metamaterials fabricated by AM have been shown to exhibit stable SE response and significant recoverable deformation under cyclic loading [39]. Despite these advances, most studies on NiTi auxetic lattices focus on global mechanical properties such as stiffness, energy absorption, or actuation capability. The interaction between the temperature-dependent superelastic response of NiTi and the deformation mechanisms of auxetic architectures, particularly the role of local geometric features such as nodal fillet radii, remains comparatively less explored.

This paper investigates the mechanical characteristics of a sinusoidal re-entrant hexagonal structure fabricated from a NiTi alloy using the L-PBF technique. In particular, the present study aims to investigate the influence of the fillet radius between the sinusoidal and transversal struts, as well as the mechanical response of the auxetic structure under superelastic conditions. The material was characterised with Differential Scanning Calorimetry (DSC) analysis to determine the phase transition temperatures (PTT). Two specimens were scanned with μ-Computed Tomography (CT) to analyse the distribution and characteristics of the internal porosity. Monotonic and cyclic tests under global strain control were conducted at different strain targets and temperatures below and above the austenite-to-martensite finish temperature on dog-bone-shaped specimens to characterise the material behaviour and determine the optimal experimental conditions to enhance SE behaviour. The global strain was measured using DIC, while the test temperature (TT) was monitored using a tailored experimental setup. Three different auxetic specimens were designed by using three different fillet radii for a sinusoidal re-entrant hexagonal configuration. Monotonic and cyclic tests under global strain control were also performed on the auxetic specimens at two temperatures, RT and 65 °C, at which the bulk material exhibited the best SE performance in terms of strain recovery (about 70% of a target strain of 2%). In addition, the experimentally measured Poisson's ratio is compared with predictions from existing analytical models for re-entrant auxetic structures, to assess their applicability and limitations when extended to sinusoidal geometries. The outcomes provide useful insights for the characterisation of an AM NiTi alloy and for the design of NiTi auxetic structures manufactured by L-PBF for advanced functional applications.

2. Materials and methods

This section describes the specimens design and production processes (Section 1.1), as well as the experimental setups developed to control specimen temperature during testing and to monitor the real-time global strain for strain-controlled cyclic tests. Specifically, the monitoring of the global strain was achieved through a Digital Image Correlation (DIC) algorithm based on the open-source Python-based toolkit μDIC developed by Olufsen et al. in 2020 [40]. The experimental setup and the algorithm designed to control the cyclic tests by the strain measured through DIC are presented in Section 1.2. The temperature monitoring setup is described in detail in Section 1.3.

2.1. Specimens design, material, and manufacturing process

2.1.1. Dog-bone specimens for material response characterisation

The selected SMA was Ti-50.6 at.% Ni. 2D dog-bone-shaped specimens were manufactured to characterise the thermo-mechanical behaviour of the material, specifically to determine the elastic moduli of austenite and martensite at different temperatures, as well as the phase transition stresses and the SE behaviour. The geometry of the tested specimens, along with its characteristic dimensions, including the cross-section, the gauge length, and the fillet radius are reported in Fig. 1a.

The specimens were heat-treated to homogenise the material properties; specifically, they were aged at 300 °C for 4 h and then water-quenched. The adopted furnace was a Nabertherm NAT 15/65 I. A Netzsch DSC 3500 Sirius differential scanning calorimeter (DSC) was used to study the alloy's transformation behaviour and to measure the PTTs. The temperature range was $-150^{\circ}C$ to $150^{\circ}C$, and the heating/cooling rate was 10 $^{\circ}C$/min.

2.1.2. Design and manufacturing of the auxetic specimens

The sinusoidal re-entrant hexagonal auxetic structure was first introduced by Dolla in 2007 [41] who proposed its use for stent application and was later investigated by Xu [42] who modelled the relationship between geometric parameters and dynamic impact response. Three different geometries were designed to investigate the role of the fillet radius in the auxetic behaviour of a 2D sinusoidal hexagonal re-entrant auxetic cell. This structure was selected because the sinusoidal profile and the presence of fillet radii reduce stress and strain concentrations at the nodes compared to sharp re-entrant geometries, thereby promoting more uniform deformation of the structure [43]. This aspect is particularly relevant for NiTi alloys, whose SE response is strongly influenced by strain localisation.

The specimens consist of a complete cell connected to the specimen bases by two half-sections; the bases are designed to be clamped in the tensile testing machine. Fig. 1b shows the main geometric parameters of the sinusoidal re-entrant structure. Three values of the fillet radius, *R*, were selected: 0, 0.5, and 1 mm. The longitudinal length *h* was appropriately adjusted to keep the geometric characteristics of the sinusoidal struts constant. The values of *R* and *h* adopted for the auxetic structures are reported in the table in Fig. 1b. The sinusoid profile is defined by the following expression:

$$y = a\sin\left(\frac{\pi}{b}x + \frac{\pi}{2}\right), x \in [0, \pi] \tag{1}$$

where a = 1.8 mm and b = 1.7 mm for all the auxetic structures.

To ensure faithful reproduction of the specimen geometry and to avoid problems associated with the L-PBF fabrication of slender specimens, each specimen type was first printed as a thick solid block using a commercial PBF-LB/M machine (Renishaw RenAM 500E), equipped with a 500 W fibre laser, which was used to produce NiTi specimens. The optimised process parameters are: laser power of 140 W, scanning speed of 700 mm/s, hatch spacing of 80 µm, and layer thickness of 30 µm. A rotated chessboard scanning pattern was used with an island of 5 x 5 mm^2 and an inter-layer rotation angle of 67°. High purity (>99.999%) argon was used to protect the building chamber. The block geometry was generated by extruding the 2D auxetic specimen profile along the build direction. The blocks were then cut perpendicular to the build direction by wire EDM on a Genesi© ECUT32D machine to obtain specimens 1 mm thick.

2.1.3. Analytical models for re-entrant auxetic structures

Different analytical models have been developed to predict the Poisson's ratio of a re-entrant hexagonal auxetic structure. Gibson and Ashby, in their pioneering work in 1982, proposed a model describing the Poisson's ratio resulting from the flexural deformation of oblique struts [2]. More advanced models have been introduced in subsequent years. For instance, Grima et al. developed an analytical formulation that considers not only flexural deformation, but also stretching and hinging of the struts [44]. These approaches are based on force and momentum equilibrium applied to beam elements. More recently, energy-based formulations have been proposed. For example, Chen et al. derived an analytical model based on an energetic description of the deformation mechanisms for re-entrant auxetic structures with sinusoidal inclusions [45].

For the auxetic structures considered in the present work, there are no analytical models directly applicable due to the presence of sinusoidal struts. Therefore, the models proposed by Gibson and Ashby and by Grima were employed by introducing appropriate geometric approximations, treating the sinusoidal struts as equivalent linear elements. For completeness, the expression for the Poisson's ratio proposed by Gibson and Ashby for an axially deformed structure is reported below:

$$\nu_{GA} = \frac{\cos^2\theta}{(h/l + \sin\theta)\sin\theta} \tag{2}$$

where θ is the angle between oblique and horizontal struts (25°), h is the transverse length of the unit cell (16 mm) and l is the length of the sinusoidal struts, which varies depending on the fillet radius R.

The expression proposed by Grima et al. is:

$$\nu_G = \frac{\sin\theta\cos^2\theta\left[\left(l_{eff}/t\right)^2 + 1 + 2\nu_m\right]}{(h/l + \sin\theta)\left[\left(l_{eff}\sin\theta t\right)^2 + 2(1+\nu_m)\sin^2\theta + \cos^2\theta\right]} \tag{3}$$

Where l_{eff} is the portion of the oblique strut most affected by the

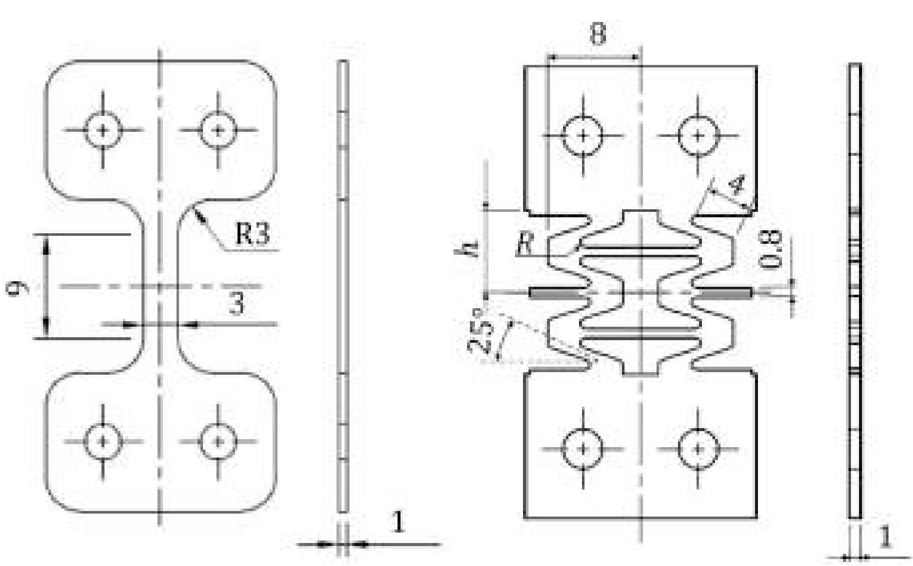

Fig. 1. Geometry and main dimensions of the specimens used in tensile testing: (a) dog-bone-shaped and (b) auxetic. All dimensions are in millimetres.

deformation (4 mm), t is the in-plane thickness of the struts (0.8 mm) and ν_m is the Poisson's ratio of the base material (0.35 based on [46]). While l_{eff} is assumed constant for all the auxetic structures, the parameter l was carefully defined to account for the presence of the fillet radius, which increases the length of the sinusoidal struts. The definition of l for each configuration is provided in Appendix A.

2.2. Tensile test experimental setup

Monotonic and cyclic tensile tests were performed at different temperatures to characterise the mechanical properties of the alloy and the auxetic structures. Reference temperatures were identified using DSC, which also determined the phase transition points. The mechanical properties of interest in this study are related to the cyclic stress–strain response of the used material. Particular focus was given to evaluating elastic moduli at different temperatures and to the evolution of cyclic residual strain. A Deben© Microtest tensile stage with a 5 kN load cell was used to perform all tensile tests. A custom 2D DIC experimental setup was developed, built, and integrated with control of the tensile stage to measure the strain field in situ during monotonic and cyclic tests. Specifically, all the cyclic tests were performed in strain control. The DIC setup includes a monochrome camera (BFS-U3-50S5M-C Blackfly S from Flir) with an Edmund Optics C Series lens (50 mm fixed focal length) and two Phottix© M200R RGB light panels with anti-flicker properties. The selection of these devices was guided by [47].

A speckled pattern was applied to the surface of each specimen before performing the tensile test. First, a thin, uniform base coat of white paint was applied, and then small black speckles were sprayed onto the surface with an airbrush, following the procedure suggested in [48]. Specifically, the white paint was Titanium White, and the black paint was Carbon Black, both from Golden High Flow Acrylics. The outcome of this procedure is shown in Fig. 2.

The square pixel edge length was approximately 16 μm. To avoid aliasing effects, speckles must span at least three pixels, and a minimum of three speckles per cell is required for the grid used in local strain computation with DIC [47]. Consequently, the minimum cell size was on the order of 100 μm, allowing for sub-millimetre spatial resolution.

Monotonic and cyclic tests were performed at a constant specimen clamping speed of 0.2 mm/min. During cyclic testing, a control algorithm (summarised in natural language in Algorithm 1) continuously acquires images of the deforming specimen, performs DIC over a selected region of interest (ROI), and computes the average axial strain. Simultaneously, the applied force is recorded. After each acquisition step, the current state is compared with a predefined target value, which may be specified in either strain or load control mode. When the difference between the measured value and the target falls below a prescribed tolerance, the target is considered achieved. Because the tensile stage operates at a low displacement speed compared to the time required for image acquisition and strain computation, this straightforward control algorithm is sufficient to ensure stable and accurate test execution.

Regarding the DIC process, an ROI and an appropriate DIC grid were defined at the beginning of the test. The first acquired image was used as the reference for computing the strain field. As the test progresses, the number of iterations required by the DIC algorithm to determine the updated grid node coordinates increases. When the number of iterations exceeds a predefined threshold (40 in this case), the reference image is updated to limit the computational cost of strain evaluation.

Camera configuration was performed using SpinView software (FLIR Systems, Inc.), and image acquisition during the tests was managed using the Spinnaker Python library. The SpinView software enables selection of camera settings and adjustment of external illumination to maximise the contrast of the speckle pattern, avoiding oversaturated spots. The exposure time was kept below 15 ms to ensure negligible distortion due to the continuous displacement applied by the tensile stage, given the displacement speed of 0.2 mm/min. Moreover, the gain and gamma factor of the camera were set equal to zero and one, respectively, to avoid the addition of artificial noise. The C++ control commands provided by the Deben Microtest tensile stage were wrapped and integrated into a Python control environment.

Algorithm 1. Computational procedure for DIC-based average strain evaluation and control during cyclic tensile tests

```
Initialise camera acquisition
Initialise communication with the tensile stage
Define initial state
for n = 1 to N_cycles do
  for half_cycle ∈ {loading, unloading} do
    Activate tensile stage actuator
    while |current_state − target_state| > tolerance do
      Acquire image frame
      Acquire force signal from tensile stage
      Perform DIC on region of interest
      Compute average axial strain
      Update current_state
    end while
    Deactivate tensile stage actuator
  end for
end for
```

2.3. Temperature control setup

SE behaviour requires the testing temperature to be higher than the A_f of the alloy. In the present study, mechanical tests were conducted at different temperatures, both below and above A_f. To ensure accurate *in situ* temperature control during tests performed above room temperature (RT), a custom temperature control system was developed. The system consisted of a set of microheaters and temperature sensors operating in a closed-loop configuration. The selected microheater was the HST. P11R0.1010.63A.2 L.020Pt Heater, while temperature was monitored

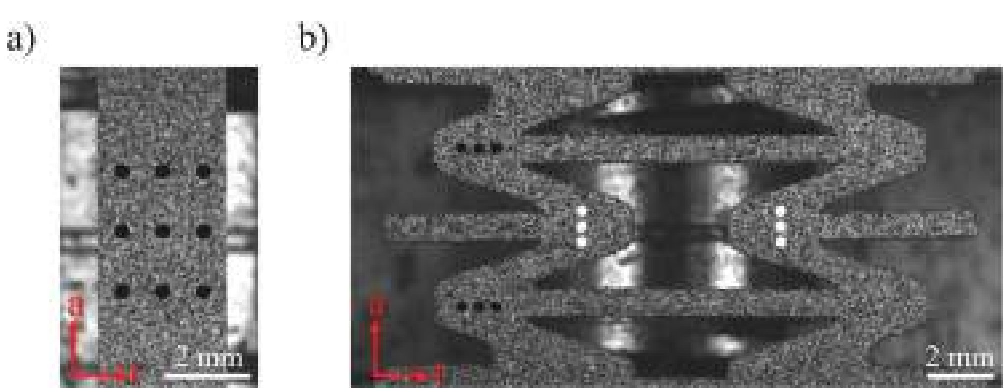

Fig. 2. An example of speckle pattern and grid applied to a) a dog-bone specimen and b) an auxetic specimen to compute the global strain through DIC during tensile tests.

using the P0K1.308.1E.B.100Pt Thin Film Measuring Resistor, both from IST AG©. The compact dimensions of the microheater (10 x 10 mm) enabled a modular arrangement, allowing construction of a heating platform that covers the specimen's lower surface. A schematic representation of the support structure (light grey) and of the microheater platform (red) integrated into the tensile stage (dark grey) is shown in Fig. 3. A specific insert was designed for each heating platform size, based on the specimen's different shapes, to secure it in the correct position on the main support. Specifically, the dog-bone-shaped specimen requires a 2-microheater platform to cover the ROI, whereas the auxetic structures use a 2x2 microheater platform (as depicted in Fig. 3).

The heating platform was secured in place using Qeeroyo© Double-Sided Thermally Conductive Tape. To reduce the grip between the platform and the specimen, the platform was first covered with Elegoo© Hi-Temp Masking Tape, and then the air gap between the platform and the specimen (visible in Fig. 3) was filled with Arctic© MX-4 Thermal Compound to ensure good heat conductivity. The gap prevented direct contact between the heating platform and the specimen, thereby protecting the brittle ceramic-covered microheaters from any applied load.

The temperature sensor, owing to its small dimensions (3 × 0.8 mm), allowed local surface temperature measurements. The temperature control algorithm was written in LabVIEW©. In a closed-loop system, the algorithm controls the power supplied to the microheaters based on the temperature signal. The temperature chain measurement includes the USB CompactDAQ chassis, NI cDAQ-9174, and the NI 9219 Universal Analog Input module, both from National Instruments©.

The microheater power supply chain consisted of a switching power supply that provides 12 V, and an IRFZ44N MOSFET, which acts as a switch and is controlled by an Arduino© Uno R4 Minima microprocessor. Thus, the transistor connects the power supply, the control signal, and the microheaters. The microheaters on the heating platform are connected in parallel to the same power supply to ensure the same voltage across each microheater.

The Arduino microcontroller generates a high-frequency square-wave signal applied to the transistor gate to regulate the voltage supplied to the microheaters. Power control is achieved via pulse-width modulation, whereby the switching frequency is kept constant, and the duty cycle, D, is adjusted. The control algorithm determines the duty cycle based on the measured temperature. The duty cycle, defined as the ratio of on-time to total period of the signal, ranges from 0 (heater permanently off) to 1 (heater continuously on). Accordingly, increasing the duty cycle increases the average power delivered to the microheaters. The control law is depicted in Fig. 4.

In the present study, target quantities are denoted with a superscript asterisk (*).

Starting from room temperature (RT), the duty cycle is initially set to a high value (D_1) to ensure rapid heating of the platform. As the measured temperature increases, the duty cycle is progressively reduced according to a linear control law. This gradual decrease in power input enables controlled temperature ramping while limiting overshoot.

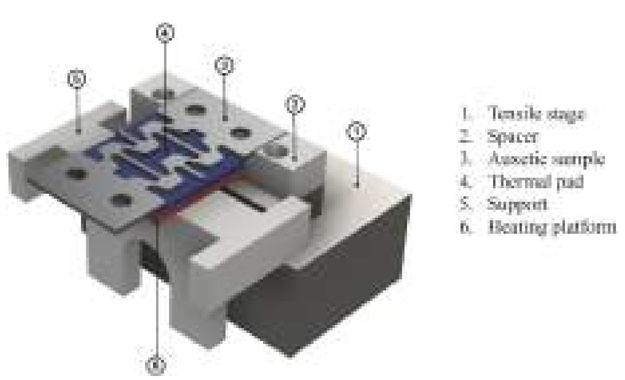

Fig. 3. Schematic illustration of the designed thermo-mechanical setup.

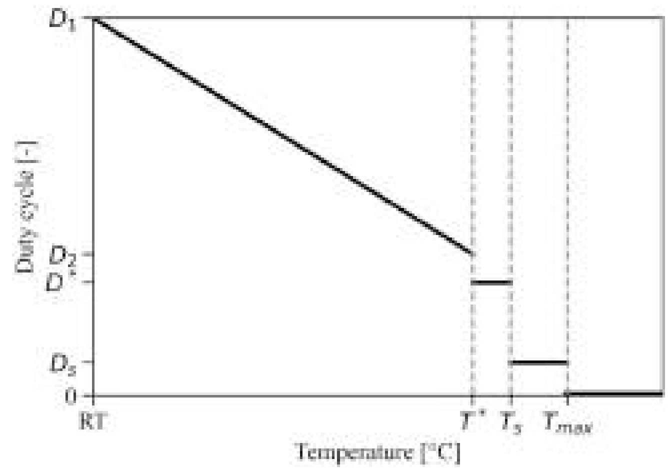

Fig. 4. Power control law of the heating experimental setup.

Once the temperature approaches the predefined target value T^*, the duty cycle is reduced to D^*, corresponding to a holding regime at which the supplied power compensates for thermal losses and stabilises the temperature around the setpoint. The threshold T_s represents an upper temperature limit beyond which additional control action is introduced. When the measured temperature exceeds T_s, the duty cycle is reduced to mitigate thermal oscillations and prevent further temperature overshoot. Beyond the maximum admissible temperature T_{max}, the duty cycle is set to zero, preventing overheating and ensuring safe operation of the microheaters and the specimen.

Fig. 5 shows an example of how the temperature sensors were positioned on the dog-bone and auxetic specimens. The central sensors are shown schematically to indicate their original position on the surface before being removed to allow DIC measurements. Once the temperature recorded by the central sensors had stabilised, they were removed, and the specimen temperature was controlled using the same scheme described previously, while also accounting for the temperature difference between the peripheral and central sensors.

3. Experimental results and discussion

This section presents the experimental results. Section 2.1 is reserved for the material thermomechanical characterisation. Section 2.2.1 presents the results of the monotonic tests while Section 2.2.2 analyse the results of the cyclic tests of the auxetic structures. DIC post-processing was performed using Ncorr, an open-source 2D-DIC MATLAB© software [49], to analyse local strain distributions and generate strain field maps, as presented in Section 2.2.1.

3.1. Material characterisation

Before testing the auxetic structures, it was necessary to characterise the NiTi alloy from a thermomechanical perspective to determine at which TTs the SE behaviour exhibits the highest strain recovery.

3.1.1. Micro-computed tomography

X-ray micro-computed tomography (μCT) analyses were carried out to evaluate the internal porosity of both the gauge volume of a dog-bone-shaped specimen and an auxetic specimen. A visual representation of the analysed volumes of both specimens is shown in Fig. 6, and the 3D reconstruction of the volumes is also reported. The reconstructed volumes were processed using *Dragonfly*© to extract pore-volume and sphericity distributions [50]. The voxels are cubic, with edge lengths of 3.0 μm and 2.8 μm for the dog-bone and auxetic specimens, respectively. The relative frequency distributions of defect volume (Fig. 7a) indicate that the two specimens exhibit comparable defect-volume ranges, with

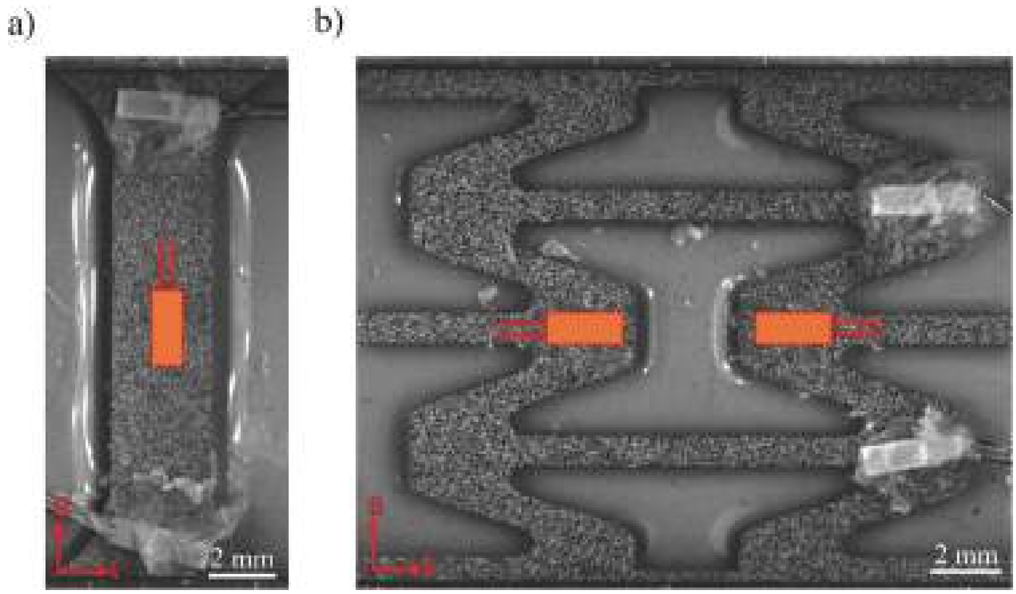

Fig. 5. (a) Dog-bone specimen and (b) auxetic specimen with applied temperature sensors. The temperature sensors are shown schematically in orange to indicate their original position before removal for DIC measurements on the specimen surface.

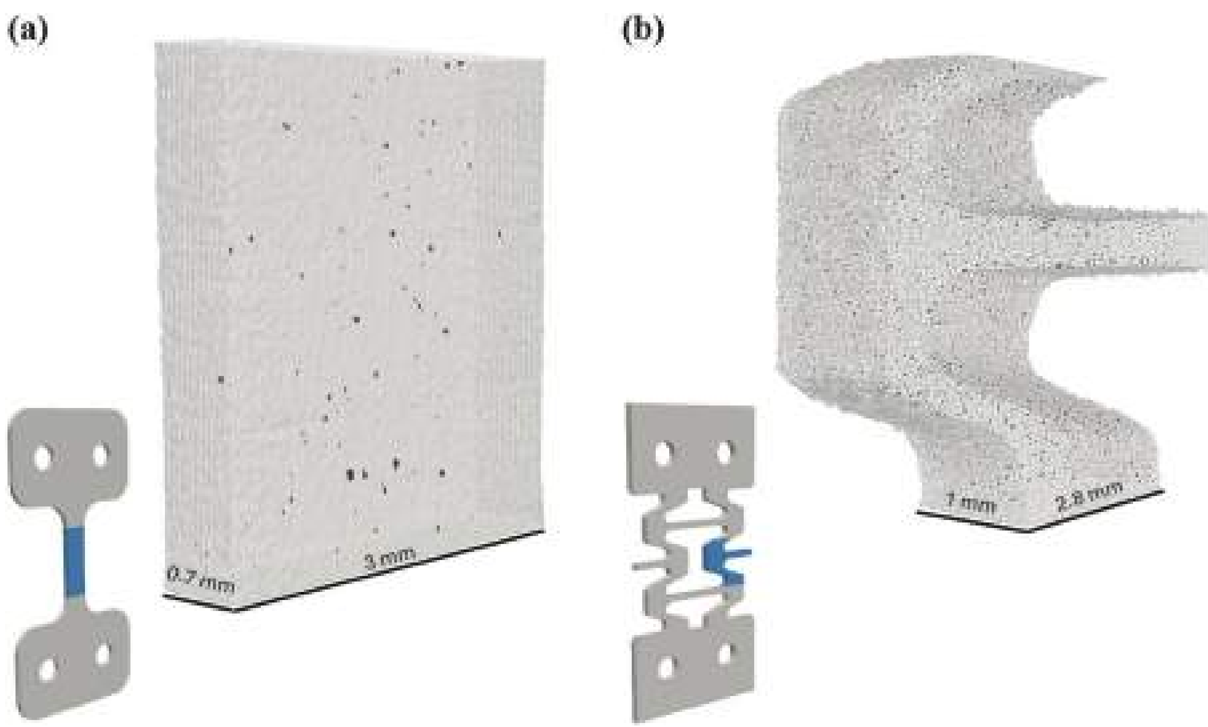

Fig. 6. μCT reconstructions of (a) dog-bone and (b) auxetic specimens with fillet radius R = 1 mm, highlighting internal porosity.

most defects characterised by volumes on the order of 10^3 μm^3. Despite the smaller analysed volume of the auxetic specimen, a greater number of defects were detected compared to the dog-bone sample. Specifically, the relative porosity was equal to 0.01% for the dog-bone specimen and 0.1% for the auxetic structure.

The relative frequency distributions of sphericity (Fig. 7b) show that the dog-bone specimen is characterised by a predominance of near-spherical defects, typically associated with gas entrapment, whereas the auxetic specimen presents a broader dispersion toward lower sphericity values.

The scatter plot of sphericity versus defect volume (Fig. 7c) further highlights that defects in the auxetic structure deviate more significantly from spherical geometry. Overall, the auxetic architecture exhibits a higher defect density and greater morphological variability, likely related to its increased geometric complexity during the L-PBF process, which may promote local strain concentrations under mechanical loading.

3.1.2. *Differential scanning calorimetry characterisation*

Differential Scanning Calorimetry (DSC) is a thermal analysis technique used to determine the phase transition temperatures (PTTs) of materials. To maintain a constant temperature ramp change during

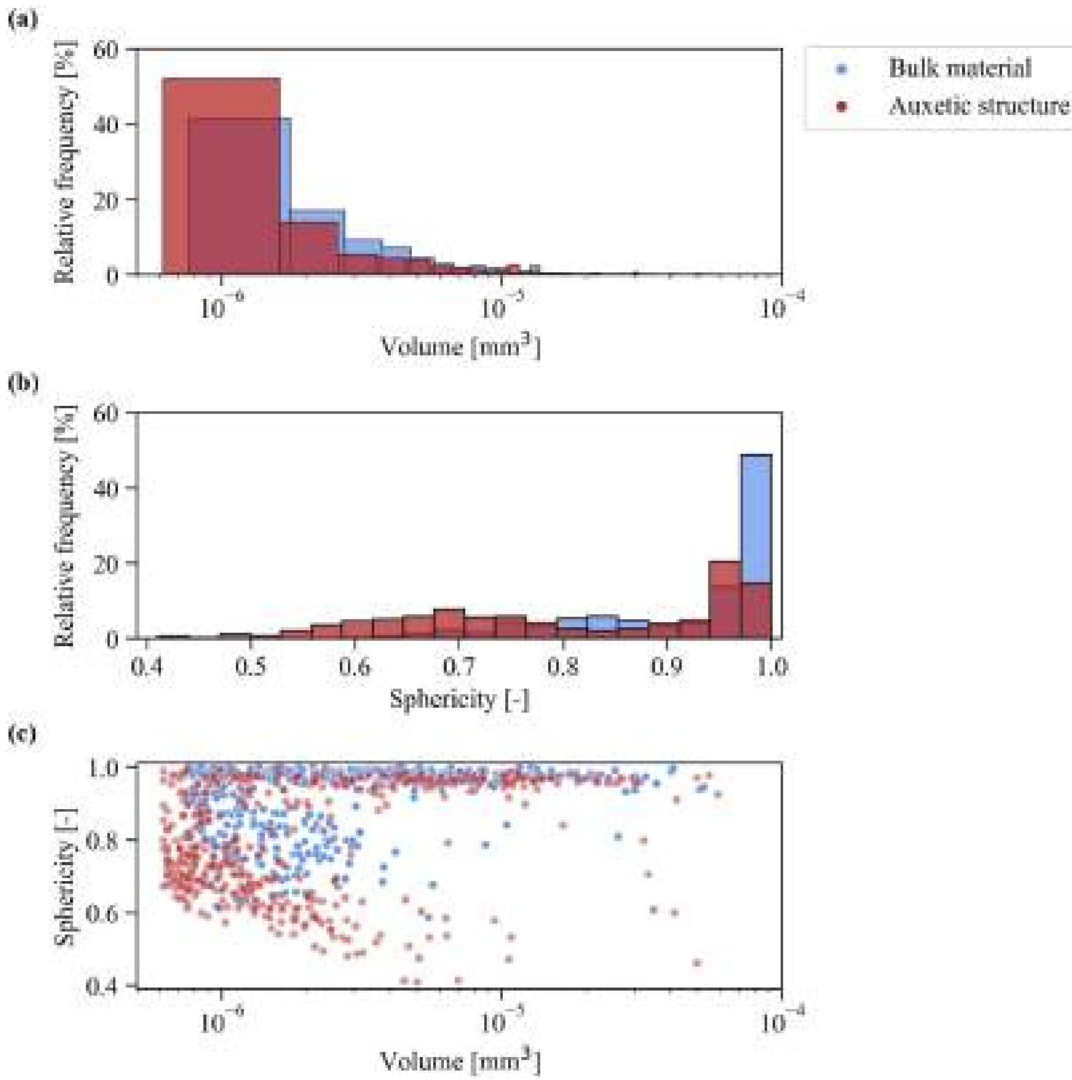

Fig. 7. Pore characterisation of dog-bone and auxetic specimens obtained by X-ray micro-computed tomography (μCT): (a) relative frequency distribution of defect volume, (b) relative frequency distribution of defect sphericity, and (c) sphericity as a function of defect volume.

testing, a variable heat flux is applied to compensate the heat release

during exothermic transformations (austenite to martensite) and

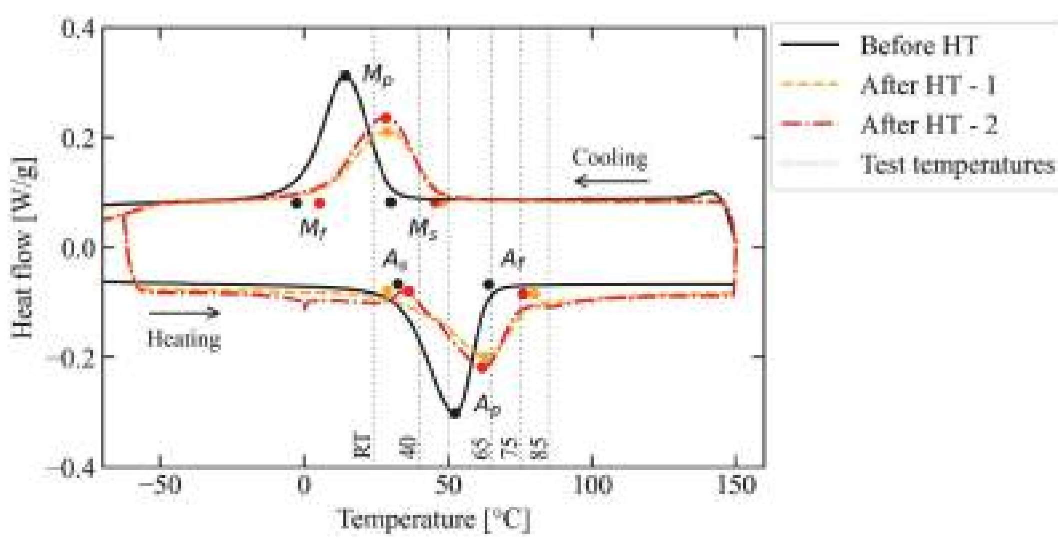

Fig. 8. DSC of the material before and after the heat treatment and test temperatures. The PTTs of each analysis are also reported with dots.

absorbed during endothermic transformations (martensite to austenite). Three DSC analyses were conducted: one on the material before the heat treatment and two on the heat-treated material. The measurements were carried out using a Mettler-Toledo© DSC 3 Stare System differential scanning calorimeter.

The heat flow – temperature curves obtained from the DSC analyses are presented in Fig. 8, while the corresponding PTTs, determined using the tangent method [29], are reported in Table 1. The presence of minor peaks and valleys during the heating process of the heat-treated NiTi alloy, particularly those observed in the 'After HT − 2′ curve, suggests the formation of secondary phases due to the heat treatment. The heat treatment resulted in a significant increase in both the martensitic and austenitic transformation temperatures.

It should be noted that the specimens were not cooled below M_f prior to mechanical testing. Therefore, the material condition at RT cannot be regarded as fully martensitic and may retain a fraction of austenite.

3.1.3. Material mechanical characterisation at different temperatures

Monotonic and strain-controlled cyclic tensile tests were performed at different temperatures to characterise the material behaviour. Specifically, the selected TTs were: room temperature (approximately 24 °C); 40 °C; 50 °C; 65 °C; 75 °C; 85 °C. Fig. 8 shows the TTs in relation to the DSC analyses. Monotonic tests to failure were performed at RT and at 65 °C. Strain-controlled cyclic tests were performed by loading the specimens to a prescribed target axial strain, ε_a^*, followed by unloading to zero force. The target strain was selected to promote superelastic recovery while limiting premature failure and excessive accumulation of irrecoverable strain. Therefore, relatively low strain targets were adopted and adjusted depending on the temperature-dependent deformation capacity observed during testing. To compare the SE response under different testing conditions, the normalised strain recovery ratio, *RR*, was adopted as the primary performance metric and defined as:

$$RR = 1 - \frac{\varepsilon_{a,r}}{\varepsilon_a^*} \tag{4}$$

Where $\varepsilon_{a,r}$ is the residual axial strain measured after complete unloading to zero force at the end of a loading–unloading cycle. For each test condition, 50 loading–unloading cycles were performed.

Initially, a single cyclic test was conducted at each temperature to identify the general trends in the material response. Based on these preliminary results, 65 °C exhibited the highest strain recovery among the investigated temperatures, as indicated by the highest RR. This condition was therefore selected for further investigation through an additional cyclic test to assess repeatability and better characterise the cyclic response under SE conditions. Specimens tested at 40 °C, 75 °C, and 85 °C (specimens 4, 8, and 9, respectively) were subsequently subjected to monotonic loading to failure after the cyclic test. These additional tests were performed to expand the experimental dataset available for material characterisation and constitutive model development. The post-cyclic monotonic responses are reported for completeness only and are not further analysed within the scope of the present study. Fig. 9a shows the monotonic tests performed at different TTs. The loading half-cycle of the first cycle of specimen 5, tested at 50 °C, is also included. Due to an experimental issue, only one cycle was completed for this specimen; the dotted line indicates that the last point does not represent failure. Fig. 9b shows the first cycles of the cyclic tests conducted at different TTs.

Fig. 10 shows the variation of the elastic modulus as a function of TT. The Young's modulus, *E*, was determined from the initial linear portion of the stress–strain curve by least-squares linear regression. For each specimen, the fitting interval was selected within the first loading branch, starting from zero strain and ending before the onset of non-linearity associated with stress-induced transformation. Depending on the specimen and testing temperature, the upper strain limit of the fitting range varied between approximately 0.11% and 0.60%. The uncertainty reported in Table 2 corresponds to the standard error of the slope obtained from the linear regression, while the coefficient of determination, R^2, was used to assess the quality of the fit. Since *E* was determined from the initial tensile loading branch, the reported values should be interpreted as apparent Young's moduli representative of the initial mechanical response under the adopted testing conditions, rather than as intrinsic phase-specific elastic constants. At RT and 65°C, where three specimens were tested, a noticeable scatter in the measured modulus was observed (Fig. 11).

The apparent Young's modulus exhibits a marked dependence on testing temperature, ranging from approximately 30 to 60 GPa.

Table 1 summarises the results of the monotonic and cyclic tests in terms of apparent Young's modulus and cyclic recovery performance, by reporting the strain recovery ratio, measured after the first and last loading–unloading cycle, RR_1 and RR_{last} respectively.

The criterion used to determine the number of cycles required for stabilisation was defined as a difference in residual strain between two consecutive cycles was lower than 1%. Specimens 2, 3, and 9a stabilised within fewer than 10 cycles, whereas specimen 7 stabilised after approximately 30 cycles. In contrast, specimen 10a did not stabilise within the duration of the test. The complete cyclic responses of specimen 7 and 8 tested at 65 °C are shown in Fig. 12.

Fig. 12 highlights the flag-like shaped response obtained at 65 °C, which is characteristic of superelastic behaviour. Compared to specimen 7, specimen 8 exhibits a more pronounced flag-like shaped hysteresis and a higher strain recovery ratio, resulting in lower residual strain accumulation during cycling. Conversely, specimen 7 shows a larger progressive shift of the hysteresis loops towards higher strain values. These observations highlight the variability of the cyclic response under nominally identical testing conditions. Such differences, as well as the scatter in the elastic moduli, may arise from several sources of variability, including microstructural heterogeneities, internal porosity and build-height-dependent variations typical of LPBF NiTi [51–53]. However, the available dataset does not allow the specific contribution of porosity to the cyclic response to be isolated or quantified. Dedicated investigations combining specimen-specific porosity characterisation and cyclic testing would be required to establish a direct correlation.

Compared to the other conditions, the material tested at 65 °C exhibits a higher initial strain recovery ratio, indicating improved superelastic (SE) performance. Based on these results, this temperature was selected as the SE TT for subsequent testing of auxetic structures.

3.2. Auxetic structure characterisation

3.2.1. Monotonic response of the auxetic structures

The characterisation of the auxetic structures was conducted through monotonic and cyclic tests at two temperatures: **RT and 65 °C**. Three monotonic tests were performed on each unit cell until the structure failed. All cyclic tests were conducted by loading the structure to 4.5% of its average axial strain and unloading to 0 N force for 50 cycles. Both axial and transverse strains were measured using DIC to compute Poisson's ratio, ν. The grids used to compute the strains are depicted in Fig. 2b. Specifically, the axial and transverse strains were computed as:

Table 1
Phase Transition Temperatures determined from the DSC analyses using the tangent method.

	Before HT	*After HT – 1*	*After HT – 2*
M_f[°C]	−2.7	5	5.4
M_p[°C]	14.1	28.7	28.4
M_s[°C]	30.1	47.9	45.4
A_s[°C]	32.5	28.5	36.2
A_p[°C]	52.4	63	61.9
A_f[°C]	64.1	79.9	76

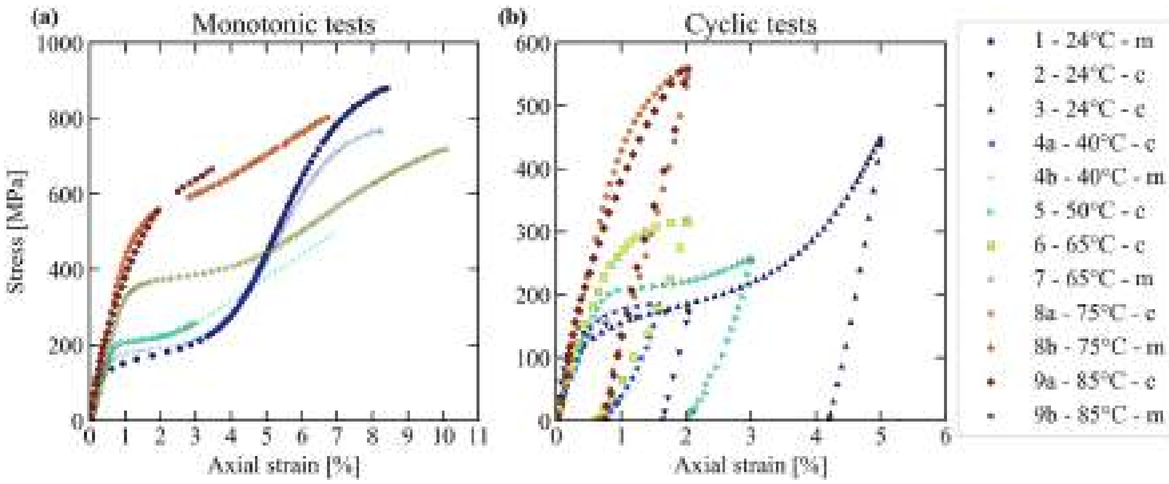

Fig. 9. Stress–strain curves obtained with a) monotonic and b) cyclic tests at different TTs. Only the first cycle of the cyclic tests is reported. The legend reports the specimen number, the TT, and the test type ('c' for cyclic and 'm' for monotonic).

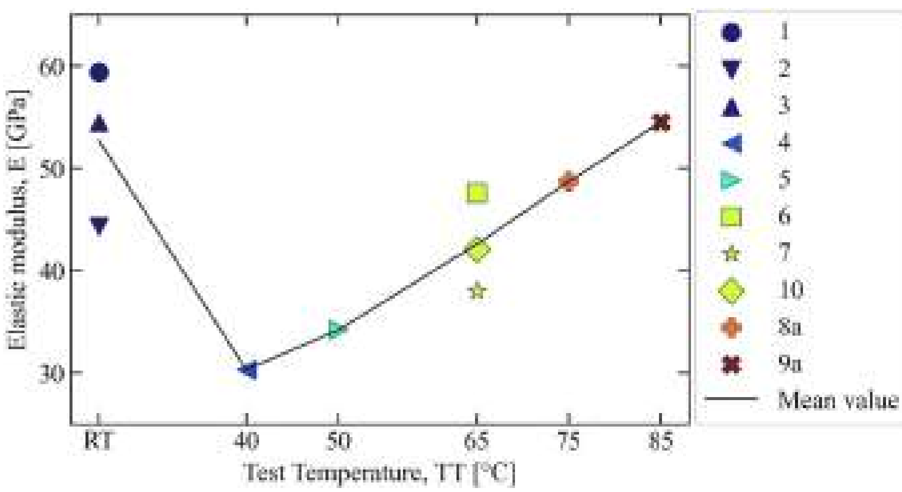

Fig. 10. Apparent Young's modulus as a function of test temperature. Symbols represent individual specimens. The solid line connects the mean value at each testing temperature.

Table 2
Summary of monotonic (m) and cyclic (c) tests, reporting TT, target axial strain (ε_a^*), elastic modulus (E) with its uncertainty (δE) and the coefficient of determination (R^2) of the linear regression. For cyclic tests, the strain recovery ratio at the first and last cycle (RR_1 and RR_{last}). The cycle number corresponding to residual strain stabilisation, N_s, is also provided.

Specimen#	*TT* [°C]	*Test*	ε_a^* [%]	*E* [GPa]	δ*E* [GPa]	R^2 [-]	RR_1 [%]	RR_{last} [%]	N_s#
1	24	m	–	54.5	±1.0	0.98	–	–	–
2	24	c	2.0	59.4	±1.6	0.99	82.8	85.8	5
3	24	c	5.0	44.3	±1.2	1.00	83.8	86.0	6
4a	40	c	1.5	30.3	±0.4	0.98	47.6	60.9	8
5	50	c	3.0	34.2	±0.1	0.99	67.7	–	–
6	65	m	–	38.0	±0.1	1.00	–	–	–
7	65	c	2.0	47.6	±1.1	0.99	30.3	42.9	32
8	65	c	2.0	42.1	±0.5	0.99	18.8	35.0	12
9a	75	c	2.0	48.7	±0.4	0.98	32.8	37.6	6
10a	85	c	2.0	54.5	±0.5	0.98	52.0	60.8	–

$$\varepsilon = \frac{1}{3}\sum_{i=1}^{3}\frac{\Delta d_i}{d_{0_i}} \quad (5)$$

Where d_{0_i} represents the initial distance between two vertically or horizontally aligned points on the grids and Δd_i is the vertical or horizontal variation in the distance between the same points.

The Poisson's ratio was evaluated as the negative derivative of a second-order polynomial fit between transverse and axial strain,

$$\nu = -\frac{d\varepsilon_t}{d\varepsilon_a} \quad (6)$$

This approach provides a smoothed estimate of the evolving ν while

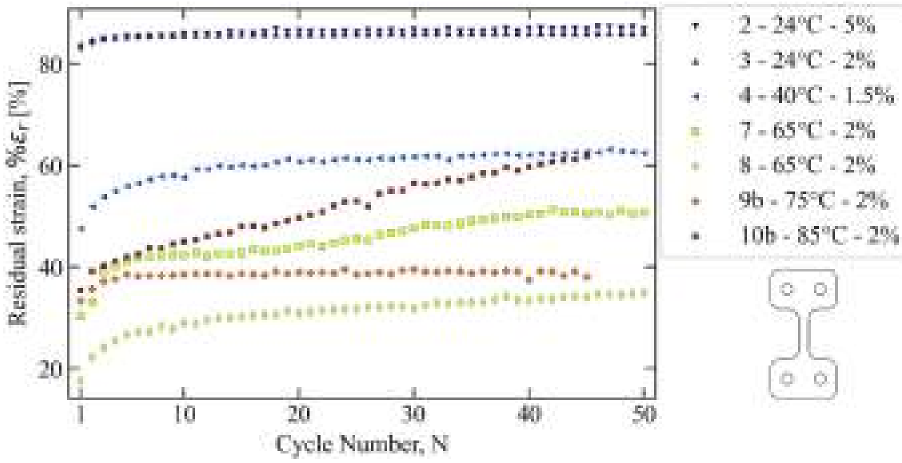

Fig. 11. Residual strain as a percentage of the strain target as a function of the number of cycles, N.

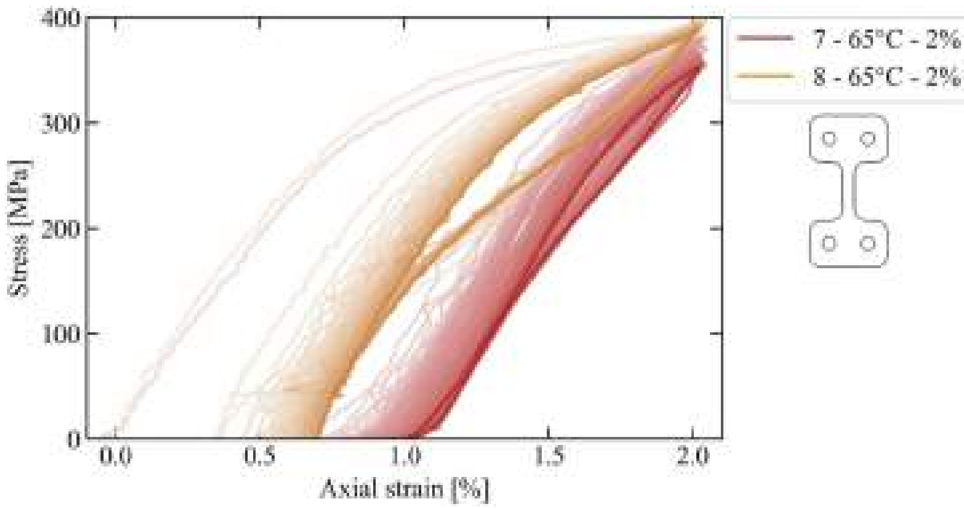

Fig. 12. Stress–strain curves of the material cyclically tested at 65°C (specimens 7 and 8).Auxetic structures mechanical characterisation.

limiting the amplification of experimental noise associated with direct numerical differentiation. As a consequence of the second-order fit, ν varies linearly with axial strain within each loading or unloading branch.

Fig. 13 summarises the average monotonic response of the auxetic structures with different fillet radii tested at RT and 65 °C. Fig. 13a reports the applied force normalised by the specimen thickness as a function of axial strain, while Fig. 13b and c show the corresponding transverse strain and Poisson's ratio evolution. For each test condition, the curves were obtained by averaging the responses of three specimens over a common strain range. The shaded bands represent the confidence intervals associated with the standard error of the mean. Owing to the architected geometry of the auxetic cells, the load-bearing cross-section varies along the structure and no representative constant area can be defined. Therefore, the applied force was normalised by the specimen thickness to provide a consistent basis for comparison among the different geometries.

To complement the strain-based representation, Fig. 14 reports the force–displacement response of the same specimens. Unlike axial strain, which is normalised by the initial cell height, the displacement provides a direct measure of the absolute deformation experienced by the structure during loading. This representation facilitates the comparison of the deformation capacity among geometries characterised by different cell dimensions.

The force responses reported in Fig. 13a and Fig. 14 clearly separate into two groups corresponding to RT and 65 °C, with the latter consistently exhibiting higher force levels irrespective of the fillet radius. This behaviour reflects the temperature-dependent mechanical response of the NiTi alloy.

While the temperature primarily affects the force level, the fillet radius mainly influences the deformation behaviour of the auxetic cell. When expressed in terms of axial strain, structures with larger fillet radius fail at lower strain values. However, the force–displacement curves show that the corresponding displacement at failure increases with increasing fillet radius. This difference arises because the cell height h increases from 5.0 mm to 9.1 mm as the fillet radius increases. Therefore, the reduction in failure strain should be interpreted in the context of the modified cell geometry rather than as a direct reduction of the absolute deformation capacity.

A different trend is observed when considering the deformation-based quantities. The axial–transverse strain curves (Fig. 13b) and the evolution of Poisson's ratio (Fig. 13c) do not group according to temperature. Instead, the results are organised into three distinct clusters associated with the three fillet radii. For a given geometry, the responses at RT and 65 °C largely overlap, while clear differences are visible between structures with $R \approx 0$ mm, $R = 0.5$ mm, and $R = 1$ mm. This indicates that the transverse deformation response and the resulting auxetic behaviour are primarily governed by the structural geometry rather than by the TT.

The DIC strain fields obtained using the open-source software Ncorr

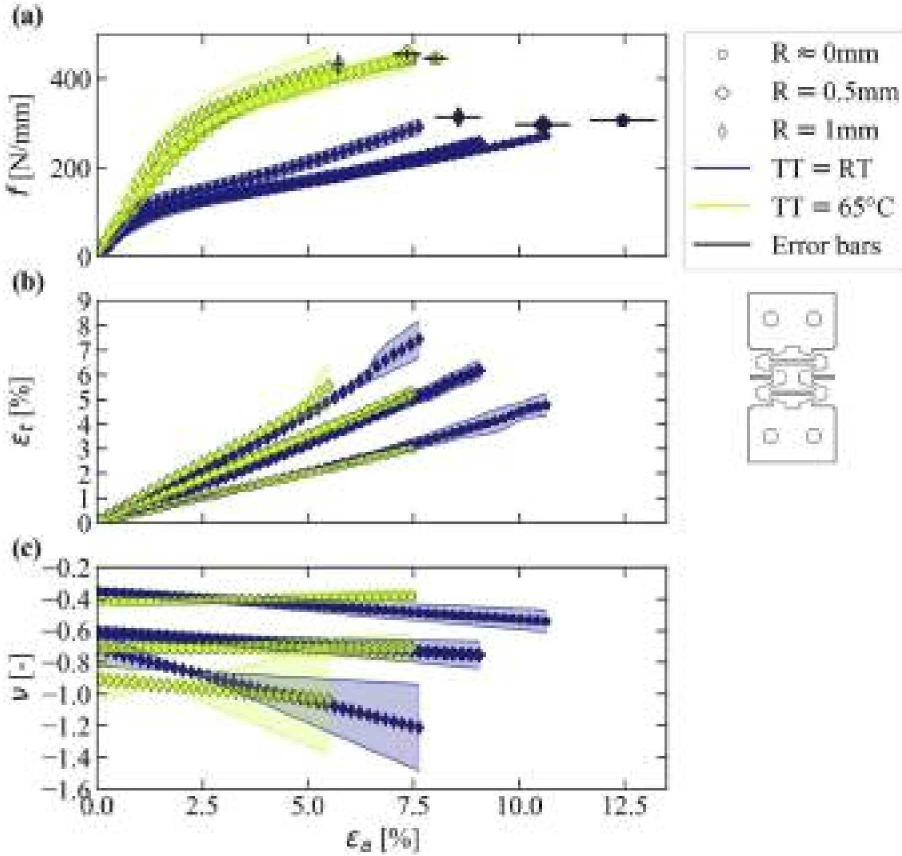

Fig. 13. Mechanical response of the auxetic structures tested under monotonic tension at RT and 65 °C for different fillet radii (R ≈ 0 mm, 0.5 mm, and 1 mm). (a) Force per unit thickness as a function of axial strain. (b) Transverse strain versus axial strain. (c) Evolution of Poisson's ratio as a function of axial strain. Solid lines represent the mean curves obtained from three specimens for each configuration, while shaded bands indicate the confidence intervals associated with the standard error of the mean. Larger markers denote the mean failure points; error bars represent ± standard error of the mean (SEM).

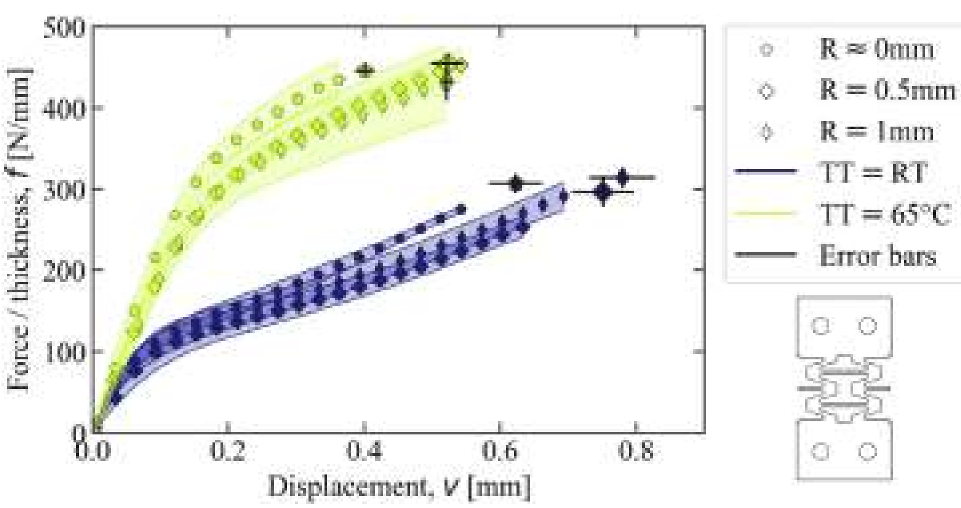

Fig. 14. Force per unit thickness as a function of absolute displacement for the auxetic structures tested under monotonic tension at RT and 65 °C for different fillet radii (R ≈ 0 mm, 0.5 mm, and 1 mm). Shaded bands indicate the confidence intervals associated with the standard error of the mean. Larger markers denote the mean failure points; error bars represent ± SEM.

and reported in Fig. 16 show that the highest strain concentrations develop near the transition region between the sinusoidal ligaments and the transverse struts. The fracture initiation points observed after testing (Fig. 16m–o) consistently coincide with these highly strained regions. For all the investigated geometries, failure initiates near the beginning of the fillet region, indicating that this area governs the onset of fracture. These observations indicate that the transition between the ligament and the transverse strut is the most critical region of the auxetic structure [54].

Fig. 15 compares the analytically predicted Poisson's ratio with the experimentally determined values. The analytical predictions were obtained using the models proposed by Gibson and Ashby and by Grima

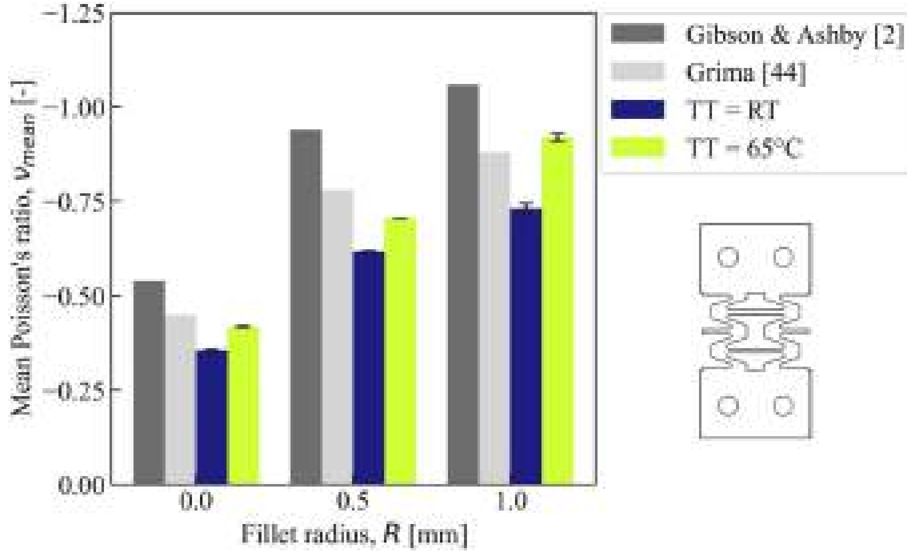

Fig. 15. Comparison between analytically predicted and experimentally measured Poisson's ratio for auxetic structures tested under monotonic tension at RT and 65°C for different fillet radii (R ≈ 0 mm, 0.5 mm, and 1 mm). Vertical black lines indicate the variability of Poisson's ratio within the elastic range.

(Eqs (1) and (2), respectively). Since these models are based on small-deformation linear-elastic assumptions, the mean Poisson's ratio was computed considering only the axial strain ranges, of 0–0.5% and 0–1% for the auxetic structures tested at RT and 65°C, respectively. Table 2 reports the percentage differences between the predicted and experimental values.

Both analytical models tend to overestimate the Poisson's ratio compared to the experimental results. The formulation proposed by Grima provides better agreement, likely due to its greater flexibility in defining the geometric parameter. In particular, it distinguishes between the overall strut length l and the portion effectively involved in deformation, l_{eff}, both of which are explicitly included in Eq. (2). Furthermore, the structures tested at 65 °C exhibit a higher Poisson's ratio in terms of absolute value compared to those tested at RT. This behaviour may be attributed to the non-negligible influence of material properties on the deformation mechanisms of the auxetic structure. Further investigation is required to fully clarify this effect (Fig. 17).

3.2.2. Cyclic response of the auxetic structures

The cyclic response of the auxetic structures is reported in Fig. 18 for RT and 65 °C. The curves are shown for the three geometries (R ≈ 0 mm, 0.5 mm, and 1 mm) and for both cyclic tests conducted for each combination of geometry and temperature. Only one valid test was retained for the R = 1 mm configuration at 65 °C due to testing issues and limited specimen availability.

The transverse strain versus axial strain curves (Fig. 18a, b) and the corresponding evolution of Poisson's ratio (Fig. 18c, d) indicate a progressive stabilisation of the response with increasing number of cycles. The difference between cycle 1 and cycle 2 is visible for all geometries and temperatures. However, stabilisation occurs more rapidly for the tests conducted at RT, where cycles 25 and 50 are almost fully superimposed and closely aligned with cycle 2. At 65 °C, a slightly more gradual evolution is observed, with small but noticeable differences still present between cycles 2, 25, and 50.

At a given temperature, the transverse strain response is primarily governed by the fillet radius. For each geometry, the curves obtained at RT and 65 °C show similar overall trends, indicating that geometry plays a dominant role in defining the transverse deformation response. However, for the R ≈ 0 mm configuration at 65 °C, a significantly more scattered response is observed. This behaviour may be attributed to a reduced geometrical conformity, as this configuration is characterised by smaller features that are more sensitive to manufacturing imperfections compared to the other geometries. The Poisson's ratio was computed from the measured axial and transverse strains. First, a linear regression was applied to the transverse–axial strain curves of each half-cycle. Then, the evolution of Poisson's ratio was evaluated by computing the opposite of the derivative of the transverse strain with respect to the axial strain. In this way, a representative Poisson's ratio value was computed for each half-cycle.

As reported in Table 3: Residual axial strain (as a percentage of maximum imposed axial strain) measured after unloading at cycle 1 and cycle 50 for the auxetic structures tested at RT and 65 °C. A clear temperature effect is observed. For all geometries, the structures tested at 65 °C exhibit significantly lower residual axial strain than those tested at RT, in both the first and last cycles. At RT, the residual strain at cycle 1 ranges between approximately 62% and 70% of the imposed strain, increasing moderately by cycle 50. In contrast, at 65 °C, the residual strain at cycle 1 is substantially lower, ranging between approximately 20% and 37% of the imposed strain, and remains markedly below the RT values even after 50 cycles (Table 4).

This behaviour is consistent with the activation of the SE mechanism at 65 °C, where stress-induced martensitic transformation enables greater strain recovery upon unloading. Conversely, at RT the material response is governed by the martensitic phase, resulting in limited recoverability and higher residual deformation.

Within each temperature group, differences related to the fillet radius are also visible. The residual strain tends to increase with increasing fillet radius.

4. Conclusions

This study investigated the mechanical response of L-PBF fabricated NiTi sinusoidal auxetic structures, focusing on the combined effects of temperature, cyclic loading, and fillet radius on both structural and functional performance.

Thermomechanical characterisation of the alloy allowed the identification of testing conditions close to the austenitic transformation range, where the NiTi material exhibits enhanced superelastic response and improved strain recovery. X-ray micro-computed tomography revealed similar defect size ranges in both dog-bone and auxetic specimens, although the auxetic structures showed a higher defect density and a wider dispersion of pore sphericity, indicating a more irregular defect morphology that may promote local strain concentrations.

The experimental campaign was supported by a dedicated testing

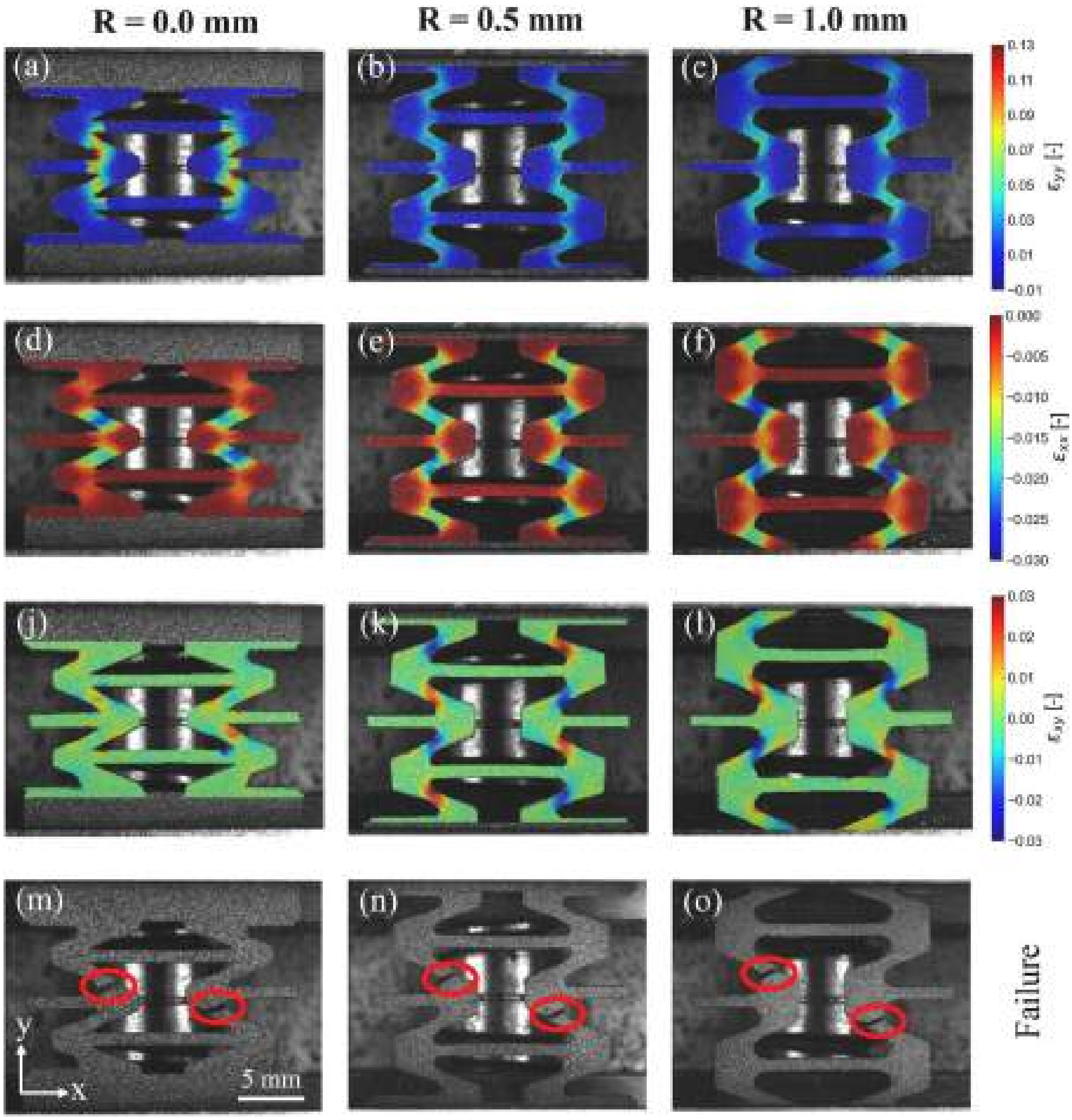

Fig. 16. DIC strain fields at maximum load for auxetic structures with fillet radii of 0.0 mm, 0.5 mm and 1.0 mm. Panels (a–c), (d–f) and (j–l) show the distributions of ε_{yy}, ε_{xx} and ε_{xy}, respectively. Panels (m–o) indicate the experimentally observed failure locations (red circles).

setup specifically developed for this study, enabling simultaneous control of specimen temperature and global strain during cyclic tests through a DIC-based feedback system.

The experimental results obtained for the auxetic structures highlight a clear distinction between material- and geometry-driven effects. Temperature mainly controls the load levels sustained by the structures, while the auxetic deformation behaviour, including transverse strain and Poisson's ratio evolution, is primarily governed by geometrical features, and particularly by the fillet radius at the nodal connections.

The fillet radius also affects the failure behaviour of the auxetic structures. While structures with smaller fillet radii exhibit higher axial strains at failure, larger fillet radii allow greater absolute displacements before fracture. DIC measurements indicate that fracture consistently initiates in the transition region between the sinusoidal ligaments and the transverse struts, identifying this area as the most critical region of the auxetic cell.

The comparison with the Gibson–Ashby and Grima analytical models shows that both formulations overestimate the auxetic response, with the latter providing better agreement. Nevertheless, they still offer a reasonable first-order estimate of the Poisson's ratio, despite being originally developed for conventional re-entrant hexagonal cells, thereby highlighting both their potential and their limitations when applied to sinusoidal geometries.

Overall, the results demonstrate that the mechanical response of the studied NiTi auxetic architectures is governed by two distinct mechanisms: temperature primarily controls the load levels sustained through an interplay between phase transformation and temperature-dependent elastic response of each phase of the alloy, whereas the auxetic response is mainly dictated by the structural geometry. Auxetic structures operating in the temperature range where the alloy exhibits SE behaviour can sustain higher loads while maintaining significant strain recovery, suggesting potential applications in adaptive architected structures and,

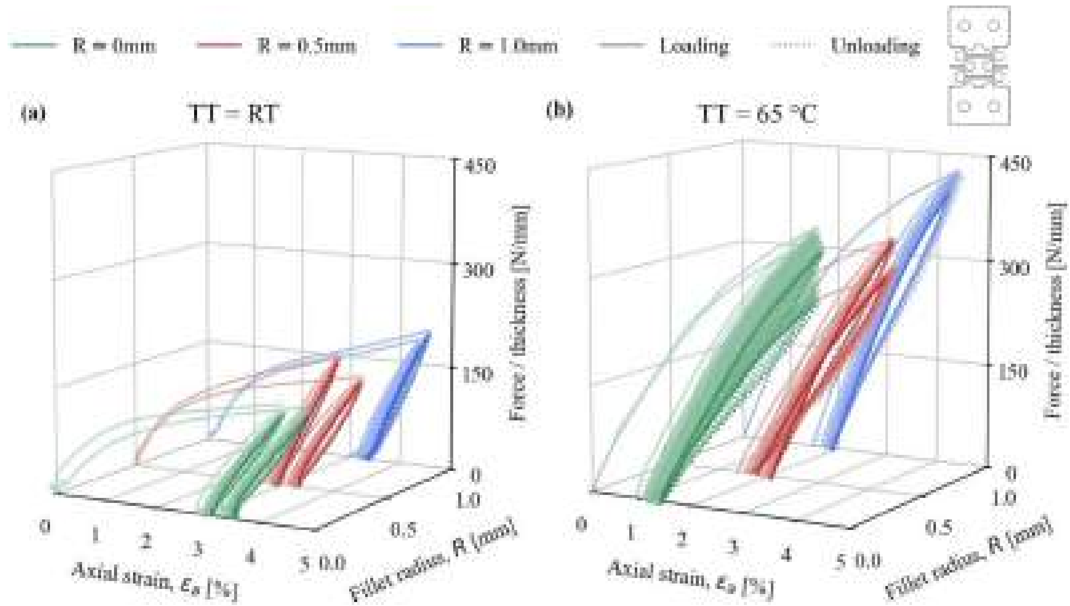

Fig. 17. Cyclic response in terms of force per thickness vs. axial strain of the structures tested at RT (a) and 65°C (b). The evolution of the cycles is indicated by a progressive increase in colour intensity. Solid and dotted lines denote loading and unloading paths, respectively.

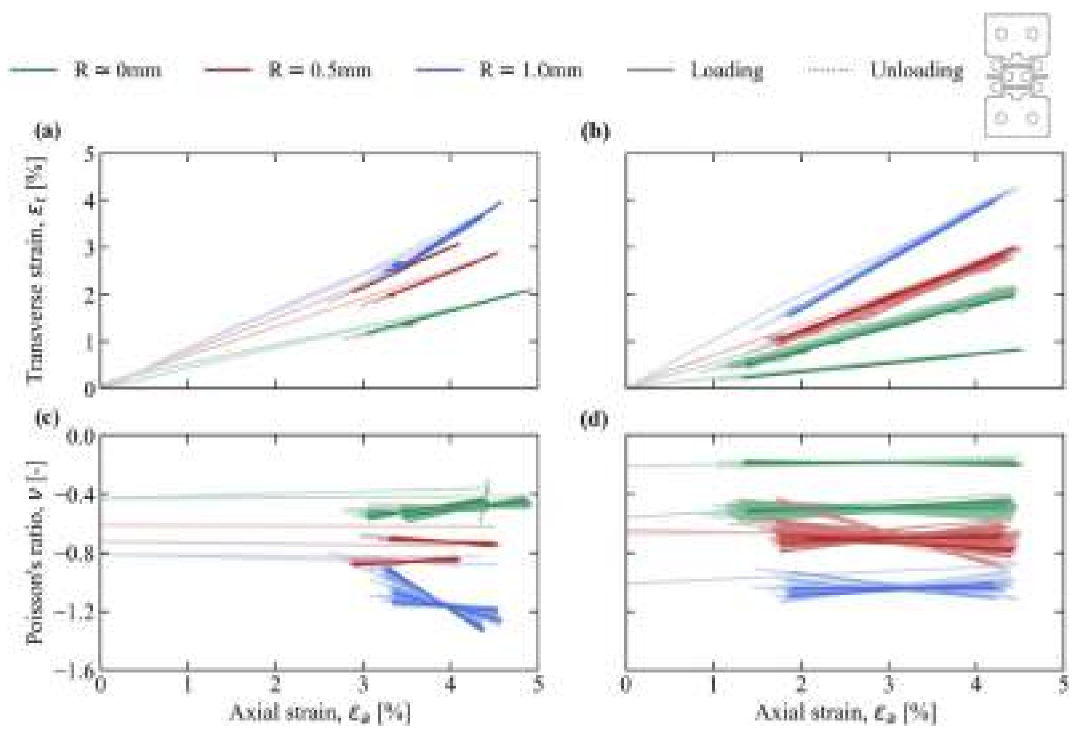

Fig. 18. Cyclic response of the auxetic structures tested at RT (a, c) and 65°C (b, d) for the three fillet radii (R ≈ 0 mm, 0.5 mm, and 1 mm). Specifically, transverse strain vs. axial strain (a, b), and Poisson's ratio vs. axial strain (c, d). The evolution of the cycles is indicated by a progressive increase in colour intensity. Solid and dotted lines denote loading and unloading paths, respectively.

with appropriate tuning of transformation temperatures, for instance, in biomedical devices employing superelastic NiTi alloys. These results also highlight the need for further optimisation of additively manufactured NiTi in order to achieve a more pronounced and stable superelastic response.

CRediT authorship contribution statement

Emanuele Avoledo: Writing – original draft, Methodology, Investigation, Formal analysis, Data curation, Conceptualization. **Xiebin Wang:** Writing – review & editing, Resources, Investigation. **Jiawen Xu:** Writing – review & editing, Resources, Methodology. **Federico Scalzo:** Writing – review & editing, Resources, Investigation. **Enrico Salvati:** Writing – original draft, Supervision, Methodology, Investigation, Funding acquisition, Conceptualization.

Table 3
percentage difference between the mean Poisson's ratio experimentally measured and the analytically predicted.

R [mm]	TT [°C]	$\Delta\nu_{GA}$ [%]	$\Delta\nu_{G}$ [%]
0.0	RT	34	21
	65	23	7
0.5	RT	34	21
	65	25	10
1.0	RT	31	17
	65	13	−5

Table 4
Residual axial strain (as a percentage of target axial strain, $\varepsilon_a{}^*$) measured after unloading at cycle 1 and cycle 50 for the auxetic structures tested at RT and 65 °C.

TT [°C]	R[mm]	$\varepsilon_{a_{r,1}}/\varepsilon_a{}^*$ [%]	$\varepsilon_{a_{r,last}}/\varepsilon_a{}^*$ [%]
RT	~0.0	62.4	68.5
	0.5	66.3	74.2
	1.0	69.6	75.6
65	~0.0	19.7	32.0
	0.5	37.0	46.0
	1.0	33.0	46.0

Declaration of competing interest

The authors declare that they have no known competing financial interests or personal relationships that could have appeared to influence the work reported in this paper.

Acknowledgments

The authors would like to acknowledge Andrea Favero for his preliminary contribution during his Master’s thesis; Hao Jiang for performing DSC analysis on the AM NiTi specimens; Lara Manzocco and Marco Lopriore for DSC analysis on the thermally treated NiTi specimens; Alex Lanzutti and Francesco Sordetti for applying the heat treatment to the NiTi specimens; and Alessandro Tognan for the post-processing of the CT-scans.

Federico Scalzo would like to acknowledge the Interconnected Nord-Est Innovation Ecosystem (iNEST - PIANO NAZIONALE DI RIPRESA E RESILIENZA (PNRR) – MISSIONE 4 COMPONENTE 2, INVESTIMENTO 1.5 – D.D. 1058 23/06/2022, ECS00000043).

The Laboratory for Advanced Mechatronics (LAMA FVG) at the University of Udine is also gratefully acknowledged for its technical support. LAMA FVG is an international research center dedicated to product and process innovation, where the three universities of Friuli Venezia Giulia (Italy) collaborate to promote R&D activities at both the academic and industrial levels.

Enrico Salvati would like to acknowledge the European Research Council (ERC) for funding the ERC Starting Grant project BREAKDOWN (Grant agreement ID: 101162848)

Appendix A. Geometric parameter definition for sinusoidal re-entrant auxetic structures within the Grima model framework

The three auxetic structures were designed by keeping the geometric characteristics of the sinusoidal struts constant, while introducing a fillet between the sinusoidal struts and the linear struts. The chosen fillet radii are 0.0, 0.5 and 1.0 mm. This fillet modifies the effective axial length of the unit cell and, consequently, influences the overall Poisson’s ratio.

The Grima formulation enables the distinction between the length of the oblique strut, l and the portion of the strut most affected by deformation, l_{eff}. The fillet region, when present, is stiffer than the sinusoidal portion due to its larger cross-section. For this reason, l_{eff} is assumed to include only the sinusoidal segment of the strut and is therefore considered constant across the three different designs.

Fig. 19 illustrates a detail of the oblique sinusoidal struts for each structure. Lines AB and $A'B'$ represent the extensions of the linear struts within the fillet region, while lines CD and $C'D'$ define the boundaries between the fillet region and the sinusoidal struts. The segment EF connects the midpoints of CD and $C'D'$ and represents the effective length l_{eff}. The segment GH is obtained by extending EF until it intersects the lines AB and $A'B'$, and corresponds to the total strut length .l

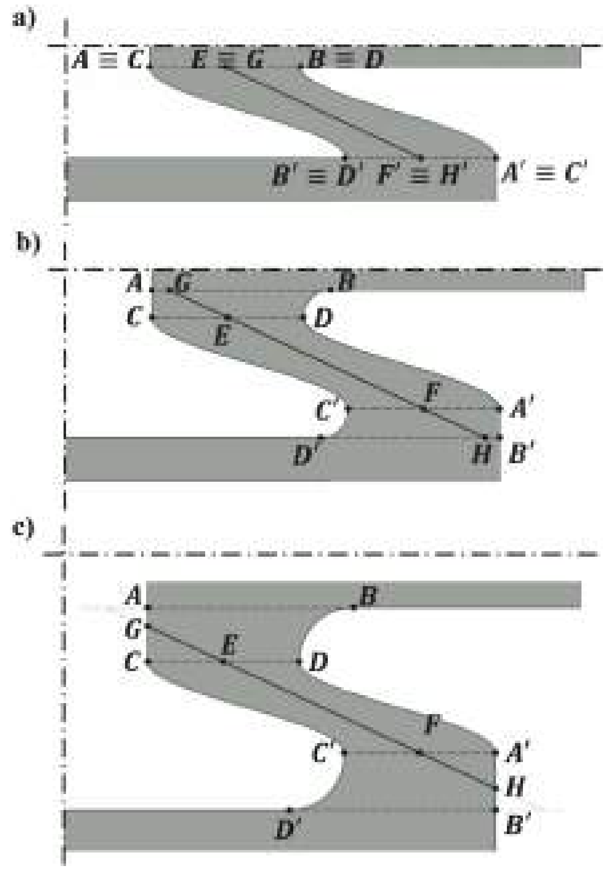

Fig. 19. Details of the sinusoidal struts and fillet region for auxetic structures with fillet radius of a) 0.0 mm, b) 0.5 mm and c) 1 mm.

Data availability

Data will be made available on request.

References

[1] A.E.H. Love, A treatise on the mathematical theory of elasticity, Cambridge University Press, 1944.
[2] L.J. Gibson, M.F. Ashby, G.S. Schajer, C.I. Robertson, The mechanics of two-dimensional cellular materials, Proc. Royal Soc. London. A. Math. Phys. Sci, 382 (1782) (1982), 25–42, doi: 10.1098/rspa.1982.0087.
[3] R. Lakes, Foam structures with a negative Poisson's ratio, Science 235 (1987) 1038–1040, https://doi.org/10.1126/science.235.4792.1038.
[4] K.E. Evans, Auxetic polymers: a new range of materials, Endeavour 15 (1991) 170–174, https://doi.org/10.1016/0160-9327(91)90123-S.
[5] Y. Zhang, W.Z. Jiang, W. Jiang, X.Y. Zhang, J. Dong, Y.M. Xie, K.E. Evans, X. Ren, Recent advances of auxetic metamaterials in smart materials and structural systems, Adv. Funct. Mater., 35(23) (2025), Art. no. 2421746, doi: 10.1002/adfm.202421746.
[6] E. Montgomery-Liljeroth, S. Schievano, G. Burriesci, Elastic properties of 2D auxetic honeycomb structures- a review, Appl. Mater. Today, 30 (2023), Art. no. 101722, doi: 10.1016/j.apmt.2022.101722.
[7] A. Yeganeh-Haeri, D.J. Weidner, J.B. Parise, Elasticity of α-cristobalite: a silicon dioxide with a negative Poisson's ratio, Science 257 (5070) (1992) 650–652, https://doi.org/10.1126/science.257.5070.650.
[8] P. Mardling, A. Alderson, N. Jordan-Mahy, C.L. Le Maitre, The use of auxetic materials in tissue engineering, Biomater. Sci. 8 (7) (2020) 2074–2083, https://doi.org/10.1039/c9bm01928f.
[9] K.E. Evans, A. Alderson, Auxetic materials: functional materials and structures from lateral thinking!, Adv. Mater. 12 (9) (2000) 617–628, https://doi.org/10.1002/(SICI)1521-4095(200005)12:9<617::AID-ADMA617>3.0.CO;2-3.
[10] A. Joseph, V. Mahesh, D. Harursampath, On the application of additive manufacturing methods for auxetic structures: a review, Adv. Manuf. 9 (3) (Sep. 2021) 342–368, https://doi.org/10.1007/s40436-021-00357-y.
[11] A. Du Plessis, N. Razavi, M. Benedetti, S. Murchio, M. Leary, M. Watson, D. Bhate, F. Berto, Properties and applications of additively manufactured metallic cellular materials: a review, Prog. Mater Sci. 125 (2022), https://doi.org/10.1016/j.pmatsci.2021.100918.
[12] M. Wallbanks, M.F. Khan, M. Bodaghi, A. Triantaphyllou, A. Serjouei, On the design workflow of auxetic metamaterials for structural applications, Smart Mater. Struct. 31 (2022), https://doi.org/10.1088/1361-665X/ac3f78.
[13] L. Mizzi, E. Salvati, A. Spaggiari, J.C. Tan, A.M. Korsunsky, Highly stretchable two-dimensional auxetic metamaterial sheets fabricated via direct-laser cutting, Int. J. Mech. Sci. 167 (2020), https://doi.org/10.1016/j.ijmecsci.2019.105242.
[14] M. Bodaghi, A. Serjouei, A. Zolfagharian, M. Fotouhi, H. Rahman, D. Durand, Reversible energy absorbing meta-sandwiches by FDM 4D printing, Int. J. Mech. Sci. 173 (2020), https://doi.org/10.1016/j.ijmecsci.2020.105451.
[15] S.S. Bagewadi, R.K. Bhagchandani, S. Manivannan, M.K. Sinha, U. Chandrasekhar, A study on the out-of-plane behavior of auxetic and hybrid auxetic structures, Prog. Addit. Manuf. 10 (9) (2025) 6935–6946, https://doi.org/10.1007/s40964-025-01018-3.
[16] K. Meena, S. Singamneni, A new auxetic structure with significantly reduced stress concentration effects, Mater. Des. 173 (2019), https://doi.org/10.1016/j.matdes.2019.107779.
[17] P. Roberjot, J.L. Herder, A unified design method for 2D auxetic metamaterials based on a minimal auxetic structure, Int. J. Solids Struct. 295 (2024), https://doi.org/10.1016/j.ijsolstr.2024.112777.
[18] Ó. Lecina-Tejero, J. Asín, J. Cuartero, M.Á. Pérez, C. Borau, Regression-guided computational design of auxetic scaffolds for soft tissue applications, Int. J. Mech. Sci. 312 (2026), https://doi.org/10.1016/j.ijmecsci.2026.111251.
[19] H.M.A. Kolken, K. Lietaert, T. van der Sloten, B. Pouran, A. Meynen, G. Van Loock, H. Weinans, L. Scheys, A.A. Zadpoor, Mechanical performance of auxetic meta-biomaterials, J. Mech. Behav. Biomed. Mater. 104 (2020), https://doi.org/10.1016/j.jmbbm.2020.103658.
[20] H. Hassanin, A. Abena, M.A. Elsayed, K. Essa, 4D printing of NiTi auxetic structure with improved ballistic performance, Micromachines 11 (8) (2020), https://doi.org/10.3390/MI11080745.
[21] H. Nguyễn, R. Fangueiro, F. Ferreira, Q. Nguyễn, Auxetic materials and structures for potential defense applications: an overview and recent developments, Text. Res. J. 93 (23–24) (2023) 5268–5306, https://doi.org/10.1177/00405175231193433.
[22] A.S. Shuaibu, J. Deng, C. Xu, V.P. Ade-Oke, A. Aliyu, D. Momoh, Advancing auxetic materials: emerging development and innovative applications, Rev. Adv. Mater. Sci., 63(1) (2024), Art. no. 20240021, doi: 10.1515/rams-2024-0021.

[23] S. Li, H. Hassanin, M.M. Attallah, N.J.E. Adkins, K. Essa, The development of TiNi-based negative Poisson's ratio structure using selective laser melting, Acta Mater. 105 (2016) 75–83, https://doi.org/10.1016/j.actamat.2015.12.017.
[24] E. Farber, A. Orlov, E. Borisov, A. Repnin, S. Kuzin, N. Golubkov, A. Popovich, TiNi alloy lattice structures with negative poisson's ratio: computer simulation and experimental results, Metals (Basel) 12 (9) (2022) Sep, https://doi.org/10.3390/met12091476.
[25] M. Sathishkumar, C.P. Kumar, S.S.S. Ganesh, M. Venkatesh, N. Radhika, M. Vignesh, A. Pazhani, Possibilities, performance and challenges of nitinol alloy fabricated by directed energy deposition and powder bed fusion for biomedical implants, J. Manuf. Process. 102 (2023) 885–909, https://doi.org/10.1016/j.jmapro.2023.08.024.
[26] Y.J. Park, H. Ahn, H. Rodrigue, Shape-memory alloy-based auxetic smart metamaterials: enabling inherently bidirectional actuation, Adv. Intell. Syst. 6 (11) (2024) Nov, https://doi.org/10.1002/aisy.202400040.
[27] K. Otsuka, K. Shimizu, Pseudoelasticity and shape memory effects in alloys, Int. Metals Rev. 31 (1) (1986) 93–114.
[28] K. Otsuka, W. Clarence Marvin, Shape memory materials, Cambridge University Press, 1999.
[29] D.C. Lagoudas, Shape memory alloys: modeling and engineering applications, Springer, 2008.
[30] J. Mohd Jani, M. Leary, A. Subic, M.A. Gibson, A review of shape memory alloy research, applications and opportunities, Mater. Des. 56 (2014) 1078–1113, https://doi.org/10.1016/j.matdes.2013.11.084.
[31] Q. Kan, Y. Zhang, W. Shi, Y. Xu, C. Yu, G. Kang, Functional fatigue of superelasticity and elastocaloric effect for NiTi springs, Int. J. Mech. Sci. 265 (2024), https://doi.org/10.1016/j.ijmecsci.2023.108889.
[32] G. Eggeler, E. Hornbogen, A. Yawny, A. Heckmann, M. Wagner, Structural and functional fatigue of NiTi shape memory alloys, Mater. Sci. Eng.: A, 378(1-2) (2004) SPEC. ISS., 24–33, doi: 10.1016/j.msea.2003.10.327.
[33] M.J. Mahtabi, N. Shamsaei, M.R. Mitchell, Fatigue of nitinol: the state-of-the-art and ongoing challenges, J. Mech. Behav. Biomed. Mater. 50 (2015) 228–254, https://doi.org/10.1016/j.jmbbm.2015.06.010.
[34] M. Elahinia, N. Shayesteh Moghaddam, M. Taheri Andani, A. Amerinatanzi, B. A. Bimber, R.F. Hamilton, Fabrication of NiTi through additive manufacturing: a review, Prog. Mater Sci. 83 (2016) 630–663, https://doi.org/10.1016/j.pmatsci.2016.08.001.
[35] Z. Pu, D. Du, D. Zhang, Z. Li, S. Xue, R. Xi, X. Wang, B. Chang, Improvement of tensile superelasticity by aging treatment of NiTi shape memory alloys fabricated by electron beam wire-feed additive manufacturing, J. Mater. Sci. Technol. 145 (2023) 185–196, https://doi.org/10.1016/j.jmst.2022.10.050.
[36] H. Jiang, W.D. Li, R. Xi, J.R. Luo, H.L. Wei, Z.H. Zhang, G.Q. Zhao, J. Van Humbeeck, R. Tao, X. Wang, Tailoring the transformation behavior and functionalities of NiTi alloy achieved by L-PBF in-situ alloying using NiTi and Ni powder mixture, Rare Met. 44 (2025) 5793–5810, https://doi.org/10.1007/s12598-025-03288-w.
[37] D. Dengiz, H. Goldbeck, S.M. Curtis, L. Bumke, J. Jetter, E. Quandt, Shape memory alloy thin film auxetic structures, Adv. Mater. Technol., 8(12) (2023), doi: 10.1002/admt.202201991.
[38] C.A. Biffi, P. Bassani, J. Fiocchi, A. Tuissi, Microstructural and mechanical response of NiTi lattice 3D structure produced by selective laser melting, Metals (Basel) 10 (6) (2020) 1–9, https://doi.org/10.3390/met10060814.
[39] C.A. Biffi, C. Soyarslan, J. Fiocchi, C. Bregoli, A. Du Plessis, A. Tuissi, M. Mehrpouya, Additive manufacturing of NiTi architected metamaterials, Addit. Manuf. Lett. 10 (2024), https://doi.org/10.1016/j.addlet.2024.100216.
[40] S.N. Olufsen, M.E. Andersen, E. Fagerholt, μDIC: an open-source toolkit for digital image correlation, SoftwareX 11 (2020), https://doi.org/10.1016/j.softx.2019.100391.
[41] W.J.S. Dolla, B.A. Fricke, B.R. Becker, Structural and drug diffusion models of conventional and auxetic drug-eluting stents, J. Med. Devices (2007), https://doi.org/10.1115/1.2355691.
[42] F. Xu, K. Yu, L. Hua, In-plane dynamic response and multi-objective optimization of negative Poisson's ratio (NPR) honeycomb structures with sinusoidal curve, Compos. Struct. 269 (2021), https://doi.org/10.1016/j.compstruct.2021.114018.
[43] K.M. Bora, S.K. Varshney, C.S. Kumar, Rounded corner thicken strut re-entrant auxetic honeycomb: analytical and numerical modeling, Mech. Res. Commun. 136 (2024), https://doi.org/10.1016/j.mechrescom.2024.104246.
[44] J.N. Grima, O. Attard, B. Ellul, R. Gatt, An improved analytical model for the elastic constants of auxetic and conventional hexagonal honeycombs, Cell. Polym. 30 (2011), https://doi.org/10.1177/026248931103000602.
[45] Z. Chen, Y. Zhou, Z. Ou, B. Wu, Z. Zhuang, Tunable in-plane mechanical properties of the novel re-entrant auxetic structure with sinusoidal inclusion, Results Eng. 28 (2025), https://doi.org/10.1016/j.rineng.2025.107546.
[46] B.S. Shariat, Y. Liu, Variation of Poisson's ratio of NiTi during pseudoelastic deformation, Shape Mem. Superelasticity 9 (4) (2023) 608–614, https://doi.org/10.1007/s40830-023-00464-8.
[47] E.M.C. Jones, M.A. Iadicola, A good practices guide for digital image correlation, Int. Digital Image Correlation Soc. (2025), https://doi.org/10.32720/idics/gpg.ed2.
[48] W.S. LePage, J.A. Shaw, S.H. Daly, Optimum paint sequence for speckle patterns in digital image correlation, Exp. Tech. 41 (5) (2017) 557–563, https://doi.org/10.1007/s40799-017-0192-3.
[49] J. Blaber, B. Adair, A. Antoniou, Ncorr: open-source 2D digital image correlation matlab software, Exp. Mech. 55 (6) (2015) 1105–1122, https://doi.org/10.1007/s11340-015-0009-1.
[50] E. Avoledo, M. Petruzzi, M. Pelegatti, A. Tognan, F. De Bona, M. Pressacco, R. Toninato, E. Salvati, Defect analysis by computed tomography in metallic materials: optimisation, uncertainty quantification and classification, Precis. Eng. 97 (2026) 235–248, https://doi.org/10.1016/j.precisioneng.2025.09.008.
[51] K. Otsuka, X. Ren, Physical metallurgy of Ti-Ni-based shape memory alloys, Prog. Mater Sci. 50 (5) (2005) 511–678, https://doi.org/10.1016/j.pmatsci.2004.10.001.
[52] A.M. Tehrani, H. Shahrokhshahi, N. Parvin, J. Brgoch, Influencing the martensitic phase transformation in NiTi through point defects, (2015), arXiv:1504.08242.
[53] P. Rocco, S. Vanaei, M. Avateffazeli, P. Bayati, M.R. Nematolahi, M. Elahinia, Investigating the effect of build height on the mechanical and functional properties of additively manufactured NiTi shape memory alloys by LPBF method, J. Alloys Comp. Commun. 10 (2026), https://doi.org/10.1016/j.jacomc.2026.100168.
[54] A. Nazir, A. Bin Arshad, C.P. Hsu, J.Y. Jeng, Effect of fillets on mechanical properties of lattice structures fabricated using multi-jet fusion technology, Materials, 14(9), (2021), doi: 10.3390/ma14092194.